Heliyon 10 (2024) e23589

Contents lists available at ScienceDirect

Heliyon

journal homepage: www.cell.com/heliyon

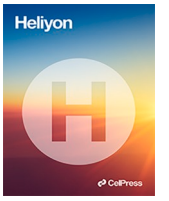

# A ROS-responsive microsphere capsule encapsulated with NADPH oxidase 4 inhibitor ameliorates macrophage inflammation and ferroptosis

Jinze Zhen [a,1], Tianhao Wan [a,1], Guangxin Sun [b,1], Xinwei Chen [a,**], Shanyong Zhang [a,*]

[a] *Department of Oral Surgery, Shanghai Ninth People's Hospital, Shanghai Jiao Tong University School of Medicine; College of Stomatology, Shanghai Jiao Tong University; National Center for Stomatology; National Clinical Research Center for Oral Diseases; Shanghai Key Laboratory of Stomatology; Shanghai Research Institute of Stomatology, Shanghai, 200011, China*

[b] *Department of Oral and Maxillofacial Surgery, School of Stomatology, China Medical University, Oral Diseases Laboratory of Liaoning, Shenyang, 110000, China*

ARTICLE INFO

*Keywords:*
Biomaterials
Nanoparticles
NOX4
Macrophage inflammation
Ferroptosis

ABSTRACT

Inflammatory macrophages within the synovium play a pivotal role in the progression of arthritis inflammation. Effective drug therapy targeting inflammatory macrophages has long been a goal for clinicians and researchers. The standard approach for treating osteoarthritis (OA) involves systemic treatment and local injection. However, the high incidence of side effects associated with long-term drug administration increases the risk of complications in patients. Additionally, the rapid clearance of the joint cavity poses a biological barrier to the therapeutic effect. NADPH oxidase 4 (NOX4) is an enzyme protein regulating the cellular redox state by generating reactive oxygen species (ROS) within the cell. In this study, we designed and fabricated a hydrogel microsphere consisting of methyl methacrylate (MMA) and polyvinyl acetate (PVA) as the outer layer structure. We then loaded GLX351322 (GLX), a novel selective NOX4 inhibitor, into hydrogel microspheres through self-assembly with the compound polyethylene glycol ketone mercaptan (mPEG-TK) containing a disulfide bond, forming nanoparticles (mPEG-TK-GLX), thus creating a two-layer drug-loaded microspheres capsule with ROS-responsive and slow-releasing capabilities. Our results demonstrate that mPEG-TK-GLX@PVA-MMA effectively suppressed TBHP-induced inflammation, ROS production, and ferroptosis, indicating a promising curative strategy for OA and other inflammatory diseases in the future.

## 1. Introduction

Inflammatory macrophages within the synovium play a pivotal role in the progression of arthritis inflammation. Clinicians and researchers have long pursued effective drug therapies targeting these inflammatory macrophages. Current approaches for treating osteoarthritis (OA) typically involve systemic treatments and local injections. However, the prolonged administration of drugs carries

* Corresponding author.
** Corresponding author.
*E-mail addresses:* chenxinwei@sjtu.edu.cn (X. Chen), zhangshanyong@126.com (S. Zhang).
[1] These authors contributed equally.

https://doi.org/10.1016/j.heliyon.2023.e23589
Received 13 August 2023; Received in revised form 15 November 2023; Accepted 7 December 2023
Available online 12 December 2023

a high risk of gastrointestinal and cardiovascular complications [1,2]. Moreover, the rapid clearance of drugs from the joint cavity presents a significant biological barrier to achieving therapeutic efficacy. Studies have revealed that the average half-life of most drugs in the joint cavity is merely 2–4 h, severely limiting their retention time and therapeutic impact [3,4].

In recent years, injectable hydrogels have been widely developed with good biocompatibility and controllable drug release [5]. Unlike traditional hydrogels, the spherical shape and uniform size of hydrogel microspheres significantly enhance injectable properties [6]. In addition, the fluidity and flexibility of the microspheres allow them to be fully dispersed in solution [7]. Methacrylate gelatin (GelMA) hydrogel microspheres prepared by microfluidic technology have been widely reported for their enhanced structural stability, uniform size and high injectivity [8,9]. Polyvinyl acetate (PVA) is a bio-friendly polymer with mechanical properties similar to cartilage, and excellent hydrophilic properties [10–12]. However, hydrogels prepared by repeated freezing will degrade quickly in the body, due to their easy solubility in water. Therefore, we attempted to modify PVA with methyl methacrylate (MMA) in the current study. The hydroxyl group on PVA could react with the ester group of MMA, resulting in reduced hydrolysis performance of PVA. Additionally, the double bond on MMA can undergo photocrosslinking under the catalysis of a photoinitiator, thereby enhancing the mechanical properties of PVA hydrogels [13].

NADPH oxidase 4 (NOX4) is an enzyme protein primarily located on the cell membrane and involved in intracellular redox reactions [14]. It regulates the cellular redox state by generating reactive oxygen species (ROS) such as hydrogen peroxide within the cell. Recent studies have highlighted the significant role of NOX4 in ferroptosis, a form of regulated cell death, by modulating the iron metabolism pathway through the production of ROS [15]. Furthermore, NOX4 also impacts the initiation and development of ferroptosis by regulating the cellular redox state [16]. Therefore, targeting NOX4 appears an effective strategy to modulate inflammation, oxidatative stress and ferroptosis, especially in inflammatory macrophages.

In this study, we loaded GLX351322 (GLX), a novel selective NOX4 inhibitor, into hydrogel microspheres through self-assembly with the compound polyethylene glycol ketone mercaptan (mPEG-TK) containing a disulfide bond, forming nanoparticles (mPEG-TK-GLX). The combination of PVA-MMA and mPEG-TK-GLX makes it an ideal candidate for ameliorating macrophage inflammation and ferroptosis, with a sustained release effect due to the ROS-responsive property of mPEG-TK [17]. Our findings demonstrated that mPEG-TK-GLX@PVA-MMA effectively suppressed inflammation, reactive oxygen species (ROS) production, and ferroptosis in inflammatory macrophages induced by *tert*-Butyl hydroperoxide (TBHP) (Fig. 1). This novel approach provides a promising strategy for the treatment of osteoarthritis (OA).

## 2. Materials and methods

### 2.1. Reagents

mPEG-TK was purchased from Ruixi Biotechnology (Xi'an, Shaanxi, China). Fetal bovine serum (FBS), and minimal essential medium alpha (α-MEM) were purchased from Cytiva (Logan, UT, USA). The Cell Counting Kit-8 (CCK-8) was obtained from Beyotime Biotechnology (Shanghai, China). Tert-Butyl hydroperoxide (TBHP) was purchased from Macklin (Shanghai, China).

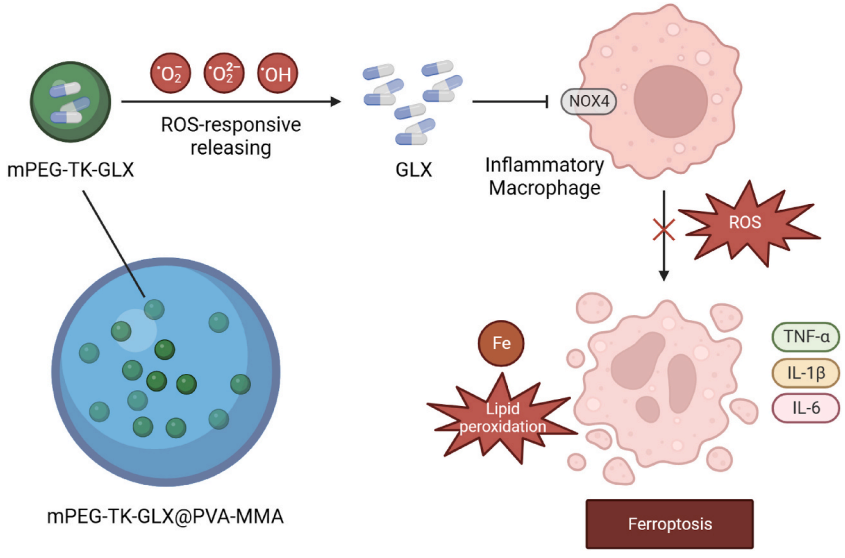


**Fig. 1.** Schematic representation of the potential application of mPEG-TK-GLX@PVA-MMA to mitigate macrophage inflammation and ferroptosis (created with BioRender.com).

### 2.2. Preparation of PVA-MMA

10 g PVA was added into 100 mL deionized water, then heated to 100 °C. The solution was stirred to dissolve, and cooled to room temperature after complete dissolution. After adjustment of pH value to 8, then the solution was heated to 60 °C. 1.84 mL of MMA solution was added dropwise, and stirred for 4 h, then cooled to room temperature. The reaction solution was dialyzed for 3 days with an 8000 KD dialysis bag to remove unreacted MMA. After dialysis, the solution was freeze-dried to obtain PVA-MMA with double bonds. Then the product was characterized by $^{1}$H NMR.

### 2.3. Preparation of mPEG-TK-GLX

20 mg GLX and 200 mg mPEG-TK was dissolved in 1 mL DMSO, respectively. 10 mL ultrapure water was added to the glass bottle, and 200 μL of mPEG-TK was firstly added under ultrasonication, followed by the dropwise addition of 200 μL GLX. The mixture was sonicated for 1.5 h and then stirred overnight in a fume hood. The prepared sample solution was added into a 3000 KD dialysis bag for dialysis to remove DMSO. After the dialysis, the solution was freeze-dried to obtain mPEG-TK-coated nanoparticles of GLX. The morphology, composition and particle size of nanoparticles by were analyzed.

The mPEG-TK-GLX was dissolved in DMSO and the encapsulated GLX was measured by UV–vis maximum absorbance (324 nm) through standard curve. The loading content and encapsulation efficiency of GLX were calculated as follows:

$$\text{Loading content} = (\text{weight of loaded drug/weight of mPEG-TK-GLX}) \times 100\%$$

$$\text{Encapsulation efficiency} = (\text{weight of loaded drug/total drug}) \times 100\%$$

### 2.4. Syntheis of mPEG-TK-GLX@PVA-MMA

mPEG-TK-GLX@PVA-MMA was synthesized and prepared by microfluidic technology. Briefly, 1 g of PVA-MA was added into 10 mL ultrapure water, heated to 100 °C and stirred to dissolve. The solution was cooled to room temperature after complete dissolution, then 200 mg of mPEG-TK-GLX nanoparticles, was added and stirred evenly. mPEG-TK-GLX@PVA-MMA with a diameter of 100–200 μm are prepared by microfluidic technology. The microsphere morphology was characterized by SEM. The distribution of mPEG-TK-GLX@PVA-MMA was observed by fluorescence microscope. mPEG-TK-GLX@PVA-MMA were dissolved in the buffer with or without ROS to detect the release of GLX.

### 2.5. Cytotoxicity assay

For CCK-8 assay, RAW 264.7 macrophages were seeded into 96-well plates at a density of $8 \times 10^3$ cells/well, respectively. Treated with various concentrations of mPEG-TK-GLX@PVA-MMA, the cells were incubated for 24 and 48 h 10 μL of CCK-8 solution was added to each well at every time point. After 2 h incubation, the absorbance was measured at the wavelength of 450 nm.

For the live/dead staining, RAW 264.7 macrophages were cultured with various concentrations of mPEG-TK-GLX@PVA-MMA for 24 h. Then the cells were incubated with the Calcein-AM and PI solution for 15 min. The live/dead cells were observed via confocal laser scanning microscopy (CLSM, Leica TCS-SP5, DM6000-CFS).

### 2.6. Quantitative PCR analysis

RAW 264.7 macrophages were seeded in 6-well plates at a density of $5 \times 10^5$ cells/well, then cultured with 100 μM TBHP, plus GLX or mPEG-TK-GLX@PVA-MMA for 24 h. Axygen RNA Miniprep Kit (Axygen, Union City, CA, USA) was used for total RNA extraction. After reverse transcription from RNA templates, TB Green™ Premix Ex Taq™ II (Takara Biotechnology, Otsu, Shiga, Japan) was used for quantitative PCR analysis. The relative gene expression was calculated using the comparative $2^{-\Delta\Delta CT}$ method. The primer sequences are listed in Table S1.

### 2.7. Intracellular ROS and superoxide detection

RAW 264.7 macrophages were plated in confocal dishes, then cultured with 100 μM TBHP plus GLX or mPEG-TK-GLX@PVA-MMA for 24 h. Then the cells were incubated with serum-free culture medium containing 10 μM DCFH-DA probe (S0033S; Beyotime Biotechnology, China) for 20 min, or 5 μM DHE probe (HY-D0079; Med Chem Express, China) for 30 min at 37 °C. Finally, the images were captured via CLSM.

### 2.8. FerroOrange and C11-BODIPY staining

RAW 264.7 macrophages were seeded in confocal dishes, and cultured with 100 μM TBHP, plus GLX or mPEG-TK-GLX@PVA-MMA for 24 h. After that, the cells were incubated with 1 μM FerroOrange probe (F374; Dojindo, Shanghai, China) for 30 min, or 5 μM C11 BODIPY 581/591 probe (D3861; Invitrogen, Carlsbad, CA, USA) for 1 h at 37 °C. Finally, the images were captured via CLSM.

### 2.9. Intracellular mitochondrial membrane potential assay

RAW 264.7 macrophages were seeded in confocal dishes, and cultured with 100 μM TBHP, plus GLX or mPEG-TK-GLX@PVA-MMA for 24 h. After that, the cells were incubated with JC-1 Mitochondrial membrane potential assay kit (C2006; Beyotime Biotechnology, China) for 20 min at 37 °C. Finally, the images were captured via CLSM.

### 2.10. Statistical analysis

All statistical analyses were conducted with a GraphPad Prism 8.0 statistical software package. All data were presented as the mean ± standard deviation (SD). After homogeneity test of variance, differences between two groups were analyzed using unpaired Student's *t*-test (two-tailed). Results for multiple group comparisons were evaluated using one-way analysis of variance (ANOVA) with Tukey's post hoc tests. Significant differences were determined to be at $*p < 0.05$ and $**p < 0.01$.

## 3. Results and discussion

As shown in Fig. 2A, TEM showed that GLX directly dispersed in water with an amorphous state. However, after the self-assembly of GLX and mPEG-TK nanoparticles in water, uniform spherical aggregates were formed with a diameter of approximately 180 nm, which was confirmed by TEM (Fig. 2B) and DLS (Fig. 2C). After analysis, the LE and EE of GLX in mPEG-TK-GLX was about 7.8 % and 55.64 % respectively according to the UV–vis spectra. The $^1$H NMR results showed that δ = 5.99 and 5.62 are the characteristic peaks of the two hydrogens on the olefin, respectively, indicating that the PVA has been successfully modified with the double bond to obtain the PVA-MMA microspheres (Fig. S1). The degree of substitution (DS) of PVA-MA was determined as 1 % by calculating the integration of characteristic peak of methacrylate at 5.99, 5.62 ppm and the backbone of PVA at 3.8 ppm. Fig. 2D showed the morphology of the PVA-MA microspheres observed by SEM, with the compact and uniform pore size distribution of the microsphere. Fig. 2E is the fluorescence image of mPEG-TK-GLX nanoparticles loaded into PVA-MMA microspheres, indicating the successful self-assembly by microfluidic.

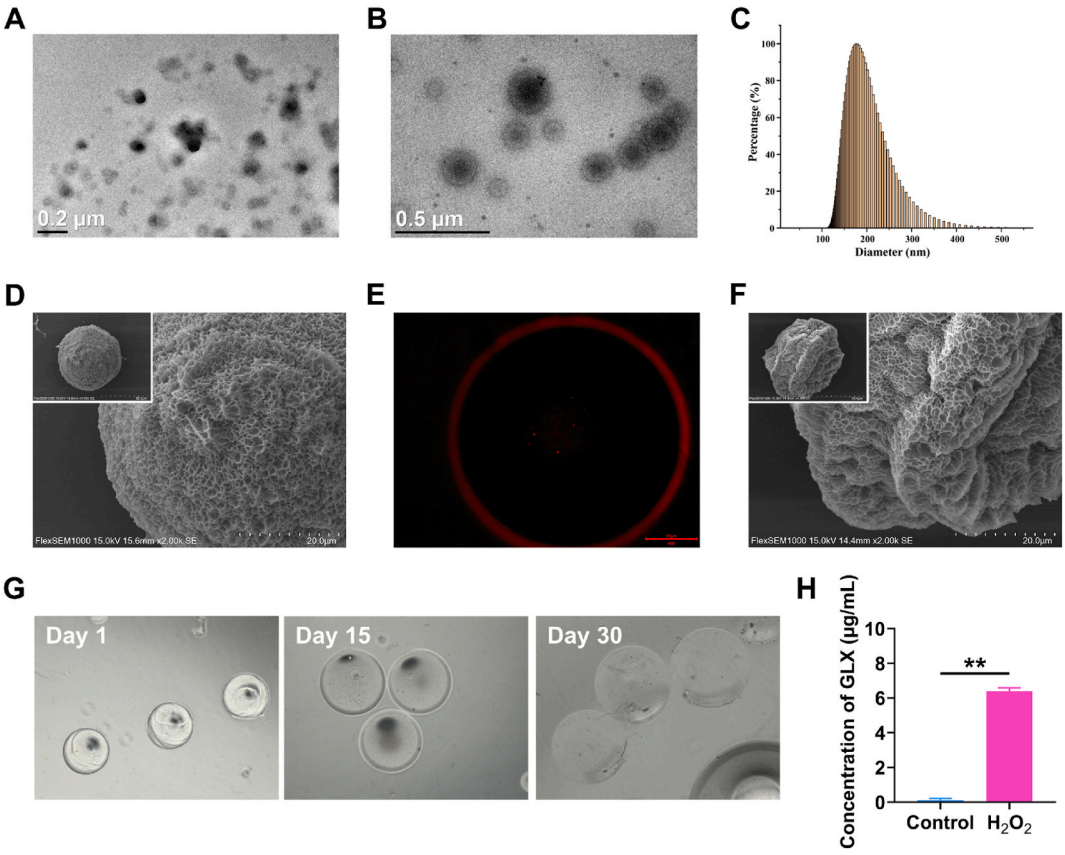


**Fig. 2.** Preparation and characterization. (A) Representative TEM images of GLX in water. (B) Representative TEM images of self-assembly between GLX and mPEG-TK in water. (C) DLS of mPEG-TK-GLX. (D) Representative SEM images of PVA-MMA microspheres. (E) Fluorescence image of mPEG-TK-GLX nanoparticles loaded into PVA-MMA microspheres after being fluorescently labeled. (F) Representative SEM images of PVA-MMA microspheres loaded with mPEG-TK-GLX. (G) Microscopic images of mPEG-TK-GLX@PVA-MMA in PBS for 1, 15, and 30 days. (H) Concentration of GLX in PBS with or without $H_2O_2$. Data represent means ± SD from three independent replicates.

Fig. 2F is the SEM images of PVA-MMA microspheres loaded with mPEG-TK-GLX nanoparticles (mPEG-TK-GLX@PVA-MMA). Because of the loading of nanoparticles, the pore size distribution of the microsphere is relatively loose and large. We next evaluated the stability of mPEG-TK-GLX@PVA-MMA in aqueous solution for 1, 15 and 30 days. The results showed that the microspheres still maintained the microsphere structure with good stability after 30 days (Fig. 2G). The ROS-responsive property was further investigated by using UV–Vis spectrophotometer. The results showed that the concentration of released GLX markedly increased after the adding of $H_2O_2$ (Fig. 2H), indicating the ROS-responsive property of mPEG-TK-GLX@PVA-MMA. Collectively, these results demonstrate mPEG-TK-GLX@PVA-MMA exhibited ROS-responsive drug releasing behavior with satisfactory stability.

We next evaluated the effect of mPEG-TK-GLX@PVA-MMA on the cell viability of RAW 264.7 macrophages. As shown in Fig. 3A and B, the live/dead staining showed that 24 h treatment of mPEG-TK-GLX@PVA-MMA hardly affected the cell viabilit in the concentration of 40 μg/mL or below, while the cell viability was jeopardized in the concentration of 80 μg/mL. The CCK-8 assay (Fig. 3C and **D**) further demonstrated that mPEG-TK-GLX@PVA-MMA hardly affected the cell viability of RAW 264.7 macrophages for 24 and 48 h, when the concentration was 80 μg/mL or below. Togther, these results indicates the satisfactory biocompatibility of mPEG-TK-GLX@PVA-MMA in the concentration of 40 μg/mL or below.

After determining the safe concentration range of mPEG-TK-GLX@PVA-MMA (40 μg/mL or below), we sought to examine its anti-inflammatory and *anti*-ROS capacity. RAW 264.7 macrophages were stimulated with 100 μg/mL TBHP for 24 h, plus GLX, mPEG-TK-GLX, mPEG-TK@PVA-MMA or mPEG-TK-GLX@PVA-MMA treatment. The RT-qPCR results (Fig. 4A) illustrated that the mRNA levels of pro-inflammatory genes, including *Tnf*, *Il1b*, and *Il6*, were upregulated with TBHP stimulation, while markedly reduced after treatment with GLX, mPEG-TK-GLX or mPEG-TK-GLX@PVA-MMA. Notably, the treatment of mPEG-TK-GLX or mPEG-TK-GLX@PVA-MMA exhibited a better inhibitory effect on pro-inflammatory genes than the treatment GLX. Furthermore, the DCFH-DA (Fig. 4B) and DHE (Fig. 4C) stainings showed that intracellular total ROS production, as well as was superoxide level, was significantly upregulated with TBHP stimulation, but markedly reduced with the treatment of GLX, mPEG-TK-GLX or mPEG-TK-GLX@PVA-MMA. Similar to the RT-qPCR results, the treatment of mPEG-TK-GLX or mPEG-TK-GLX@PVA-MMA exhibited a better inhibitory effect on intracellular total ROS and superoxide level. Taken together, these results suggest the satisfactory anti-inflammatory and *anti*-ROS performance of mPEG-TK-GLX@PVA-MMA.

Considering the relationship among the inflammatory response, oxidative stress, and ferroptosis, we next evaluated whether mPEG-TK-GLX@PVA-MMA could inhibit TBHP-induced ferroptosis in RAW 264.7 macrophages. As expected, the results of FerroOrange staining (Fig. 5A) illustrated that TBHP stimulation significantly increased the intracellular $Fe^{2+}$ level. However, the treatment of GLX, mPEG-TK-GLX or mPEG-TK-GLX@PVA-MMA eminently reduced the fluorescence of FerroOrange, suggesting the reduced intracellular $Fe^{2+}$ level. Meanwhile, we also explored the effect of mPEG-TK-GLX@PVA-MMA on lipid peroxidation. As shown in Fig. 5B, TBHP stimulation markedly increased the lipid peroxidation level, which manifested with enhanced green fluorescence (oxidized state) and reduced red fluorescence (non-oxidized state). However, the treatment of mPEG-TK-GLX@PVA-MMA exhibited the most effective inhibition on the lipid peroxidation level, with increased red fluorescence (non-oxidized state) and decreased green fluorescence (oxidized state). Multiple lines of evidences implied that increased ROS production may lead to the damaged integrity of the mitochondrial membrane, thus triggering the process of ferroptosis [18–20]. Hence, we further investigated the effect of mPEG-TK-GLX@PVA-MMA on mitochondrial membrane integrity. The results of JC-1 staining showed that TBHP stimulation reduced

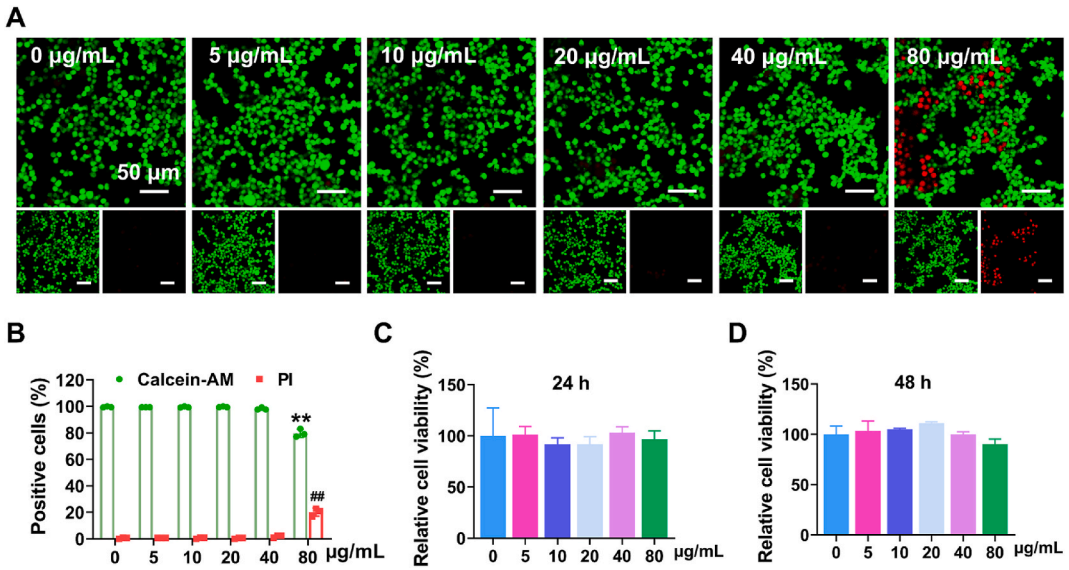


**Fig. 3.** Effect of mPEG-TK-GLX@PVA-MMA on the cell viability of RAW 264.7 macrophages. (A) CCK-8 assay for 24 h. (B) CCK-8 assay for 48 h. (C) Quantitative analysis of live/dead staining. (D) Representative confocal images of live/dead staining. Data represent means ± SD from three independent replicates.

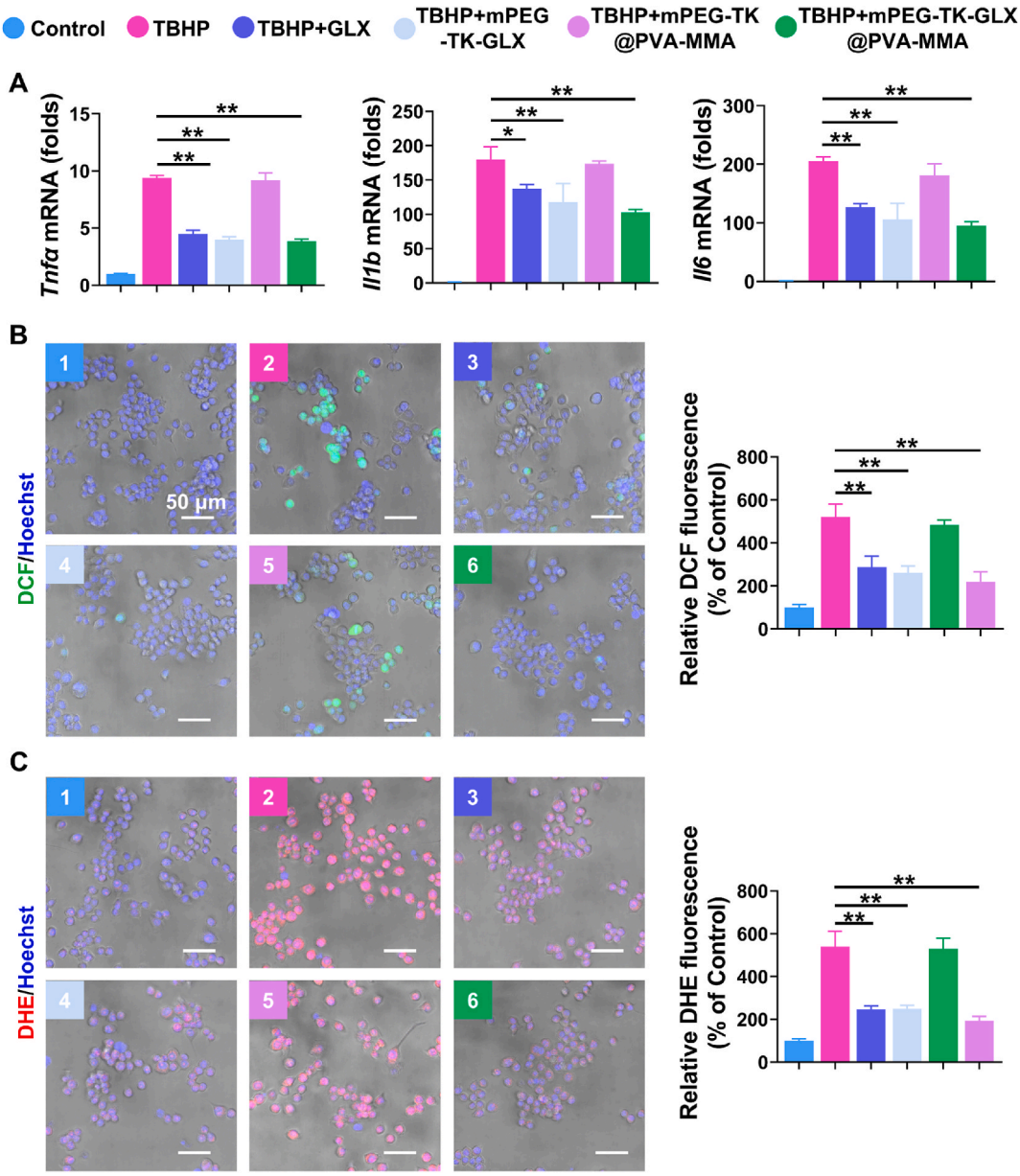


**Fig. 4.** mPEG-TK-GLX@PVA-MMA reduces TBHP-induced inflammatory response and ROS production in RAW 264.7 macrophages. (A) Expression of pro-inflammatory genes evaluated by RT-qPCR. (B) Confocal images and quantitative analysis of RAW 264.7 macrophages stained with DCFH-DA. (C) Confocal images and quantitative analysis of RAW 264.7 macrophages stained with DHE. Data represent means ± SD from three independent replicates.

the mitochondrial membrane potential of cells, with increased JC-1 monomers in green fluorescence (Fig. 5C). However, the treatment of mPEG-TK-GLX@PVA-MMA exhibited the most effective protective effect on the mitochondrial membrane potential, with increased red fluorescence (non-oxidized state) and decreased green fluorescence (oxidized state). Taken together, these results demonstrate that mPEG-TK-GLX@PVA-MMA effectively reduces TBHP-induced ferroptosis in RAW 264.7 macrophages.

## 4. Conclusions

In this study, we designed and fabricated a hydrogel microsphere composed of MMA and PVA as the outer layer structure, and then loaded the ROS-responsive nanoparticle mPEG-TK-GLX into the hydrogel microspheres to produce a two-layer drug-loaded microspheres capsule with ROS-responsive and slow-releasing ability. The results demonstrate that mPEG-TK-GLX@PVA-MMA suppressed TBHP-induced inflammation, ROS production and ferroptosis in inflammatory macrophages, providing a promising curative strategy

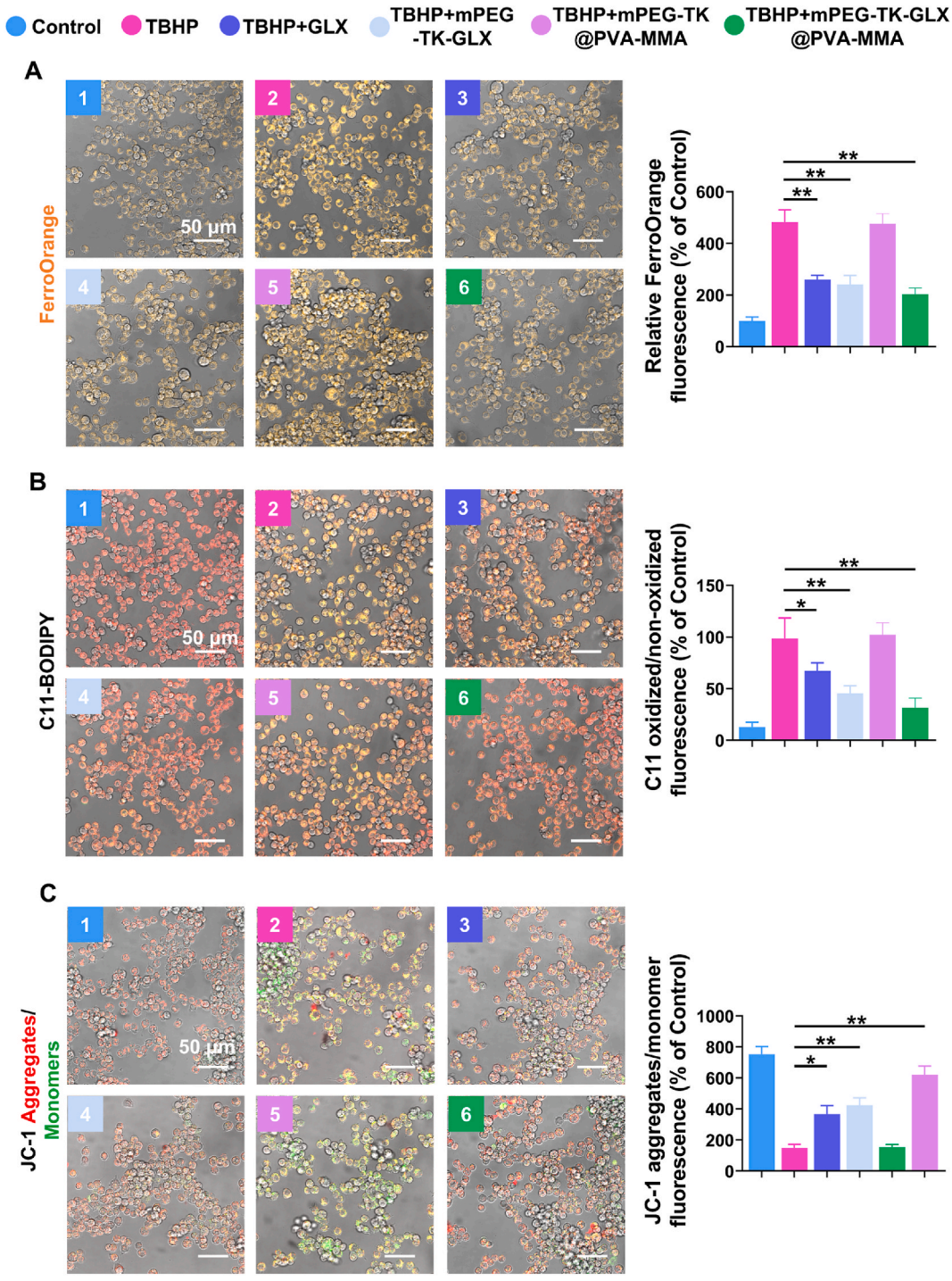


**Fig. 5.** mPEG-TK-GLX@PVA-MMA reduces TBHP-induced ferroptosis in RAW 264.7 macrophages. (A) Confocal images and quantitative analysis of RAW 264.7 macrophages stained with FerroOrange. (B) Confocal images and quantitative analysis of RAW 264.7 macrophages stained with C11-BODIPY. (C) Confocal images and quantitative analysis of RAW 264.7 macrophages stained with JC-1 mitochondrial membrane potential probe. Data represent means ± SD from three independent replicates.

for OA and other inflammatory diseases in the future.

## Data availability

Data will be made available on request.

## CRediT authorship contribution statement

**Jinze Zhen:** Conceptualization, Data curation, Formal analysis, Investigation, Methodology, Software, Writing – original draft. **Tianhao Wan:** Data curation, Formal analysis, Methodology, Software. **Guangxin Sun:** Investigation, Methodology, Software. **Xinwei Chen:** Data curation, Formal analysis, Resources, Software. **Shanyong Zhang:** Funding acquisition, Project administration, Supervision, Writing – review & editing.

## Declaration of competing interest

The authors declare that they have no known competing financial interests or personal relationships that could have appeared to influence the work reported in this paper.

## Acknowledgments

This work was financially supported by the National Natural Science Foundation of China (Grant No. 82071135).

## Appendix A. Supplementary data

Supplementary data to this article can be found online at https://doi.org/10.1016/j.heliyon.2023.e23589.

## References

[1] S.S. Laev, N.F. Salakhutdinov, Anti-arthritic agents: progress and potential, Bioorg. Med. Chem. 23 (13) (2015) 3059–3080.
[2] J.W. Bijlsma, F. Berenbaum, F.P. Lafeber, Osteoarthritis: an update with relevance for clinical practice, Lancet 377 (9783) (2011) 2115–2126.
[3] C.H. Evans, V.B. Kraus, L.A. Setton, Progress in intra-articular therapy, Nat. Rev. Rheumatol. 10 (1) (2014) 11–22.
[4] M.C. Bruno, M.C. Cristiano, C. Celia, N. d'Avanzo, A. Mancuso, D. Paolino, J. Wolfram, M. Fresta, Injectable drug delivery systems for osteoarthritis and rheumatoid arthritis, ACS Nano 16 (12) (2022) 19665–19690.
[5] T. Xin, J. Mao, L. Liu, J. Tang, L. Wu, X. Yu, Y. Gu, W. Cui, L. Chen, Programmed sustained release of recombinant human bone morphogenetic protein-2 and inorganic ion composite hydrogel as artificial periosteum, ACS Appl. Mater. Interfaces 12 (6) (2020) 6840–6851.
[6] Y.J. Seong, G. Lin, B.J. Kim, H.E. Kim, S. Kim, S.H. Jeong, Hyaluronic acid-based hybrid hydrogel microspheres with enhanced structural stability and high injectability, ACS Omega 4 (9) (2019) 13834–13844.
[7] Q. Li, B. Chang, H. Dong, X. Liu, Functional microspheres for tissue regeneration, Bioact. Mater. 25 (2023) 485–499.
[8] P. Chen, C. Xia, S. Mei, J. Wang, Z. Shan, X. Lin, S. Fan, Intra-articular delivery of sinomenium encapsulated by chitosan microspheres and photo-crosslinked GelMA hydrogel ameliorates osteoarthritis by effectively regulating autophagy, Biomaterials 81 (2016) 1–13.
[9] Z. Zhang, G. Huang, Intra-articular lornoxicam loaded PLGA microspheres: enhanced therapeutic efficiency and decreased systemic toxicity in the treatment of osteoarthritis, Drug Deliv. 19 (5) (2012) 255–263.
[10] Y. Chen, J. Song, S. Wang, W. Liu, PVA-based hydrogels: promising candidates for articular cartilage repair, Macromol. Biosci. 21 (10) (2021), e2100147.
[11] D. Jin, S. Yang, S. Wu, M. Yin, H. Kuang, A functional PVA aerogel-based membrane obtaining sutureability through modified electrospinning technology and achieving promising anti-adhesion effect after cardiac surgery, Bioact. Mater. 10 (2022) 355–366.
[12] S. Alven, B.A. Aderibigbe, Fabrication of hybrid nanofibers from biopolymers and poly (vinyl alcohol)/poly (epsilon-Caprolactone) for wound dressing applications, Polymers 13 (13) (2021).
[13] M.S. Islam, J.H. Yeum, A.K. Das, Synthesis of poly(vinyl acetate-methyl methacrylate) copolymer microspheres using suspension polymerization, J. Colloid Interface Sci. 368 (1) (2012) 400–405.
[14] B.C. Ogboo, U.V. Grabovyy, A. Maini, S. Scouten, A. van der Vliet, A. Mattevi, D.E. Heppner, Architecture of the NADPH oxidase family of enzymes, Redox Biol. 52 (2022), 102298.
[15] M.W. Park, H.W. Cha, J. Kim, J.H. Kim, H. Yang, S. Yoon, N. Boonpraman, S.S. Yi, I.D. Yoo, J.S. Moon, NOX4 promotes ferroptosis of astrocytes by oxidative stress-induced lipid peroxidation via the impairment of mitochondrial metabolism in Alzheimer's diseases, Redox Biol. 41 (2021), 101947.
[16] R. Zhou, Y. Chen, S. Li, X. Wei, W. Hu, S. Tang, J. Ding, W. Fu, H. Zhang, F. Chen, W. Hao, Y. Lin, R. Zhu, K. Wang, L. Dong, Y. Zhao, X. Feng, F. Chen, C. Ding, W. Hu, TRPM7 channel inhibition attenuates rheumatoid arthritis articular chondrocyte ferroptosis by suppression of the PKCalpha-NOX4 axis, Redox Biol. 55 (2022), 102411.
[17] X. Li, Y. Li, C. Yu, H. Bao, S. Cheng, J. Huang, Z. Zhang, ROS-responsive janus Au/mesoporous silica core/shell nanoparticles for drug delivery and long-term CT imaging tracking of MSCs in pulmonary fibrosis treatment, ACS Nano 17 (7) (2023) 6387–6399.
[18] X. Jiang, B.R. Stockwell, M. Conrad, Ferroptosis: mechanisms, biology and role in disease, Nat. Rev. Mol. Cell Biol. 22 (4) (2021) 266–282.
[19] M.Y. Liu, H.M. Li, X.Y. Wang, R. Xia, X. Li, Y.J. Ma, M. Wang, H.S. Zhang, TIGAR drives colorectal cancer ferroptosis resistance through ROS/AMPK/SCD1 pathway, Free Radic. Biol. Med. 182 (2022) 219–231.
[20] D. Zheng, J. Liu, H. Piao, Z. Zhu, R. Wei, K. Liu, ROS-triggered endothelial cell death mechanisms: focus on pyroptosis, parthanatos, and ferroptosis, Front. Immunol. 13 (2022), 1039241.